One-dimensional visible-light-driven bifunctional photocatalysts based on $Bi_4Ti_3O_{12}$ nanofiber frameworks and Bi_2XO_6 (X = Mo, W) nanosheets

Ying Liu, Mingyi Zhang*, Lu Li, Xitian Zhang**

Key Laboratory for Photonic and Electronic Bandgap Materials, Ministry of Education, School of Physics and Electronic Engineering, Harbin Normal University, Harbin 150025, People's Republic of China

ABSTRACT

Aurivillius oxide semiconductors are important photocatalysts because of their unique electronic structure and layered crystal. In this paper, two kinds of Aurivillius oxide semiconductor heterostructures based on $Bi_4Ti_3O_{12}$ nanofiber frameworks and Bi_2XO_6 (X = Mo, W) nanosheets are successfully synthesized by combining the electrospinning technique and solvothermal method. The high-resolution transmission electron microscopy results reveal that an intimate interface between $Bi_4Ti_3O_{12}$ nanofibers and Bi_2MoO_6 or Bi_2WO_6 nanosheets forms in the heterojunctions. Photocatalytic tests show that the $Bi_4Ti_3O_{12}/Bi_2XO_6$ (X = Mo, W) heterostructures exhibit enhanced photocatalytic activity than bare $Bi_4Ti_3O_{12}$ and Bi_2XO_6 (X = Mo, W) under visible light, mainly owing to the photoinduced interfacial charge transfer based on the photosynergistic effect of the $Bi_4Ti_3O_{12}/Bi_2XO_6$ heterojunction. The heterostructures can be reclaimed easily by sedimentation without a decrease of the photocatalytic activity due to the large length to diameter ratio of nanofiber frameworks. Moreover, such simple and versatile strategy can provide a general way to fabricate other heterostructures of Bi(III)-containing oxides, such as $Bi_4Ti_3O_{12}/BiVO_4$ and $Bi_4Ti_3O_{12}/BiOCl$.

© 2014 Elsevier B.V. All rights reserved.

1. Introduction

Photocatalysts could utilize solar energy to remedy environmental pollutions, thus attracting worldwide attention. To utilize solar energy more effectively, the development of efficient visible-light-driven (VLD) photocatalysts has attracted worldwide attention [1–6]. Very recently, Aurivillius oxide semiconductors are evoking interest due to their layered crystal and unique electronic structure [7–15]. The Aurivillius phases can be described as intergrowth structures composed of alternating layers of $(Bi_2O_2)^{2+}$ units with perovskite-like $(A_{n-1}B_nO_{3n+1})^{2-}$ blocks, where A is a large 12 co-ordinate cation, and B is a small 6 co-ordinate cation, $n = 1$–8. Compared to bulk photocatalysts without a layered structure, layered photocatalysts are a more favorable environment for the diffusion and separation of photoexcited electron–hole pairs. This is because the oxidation and reduction sites exist in an isolated fashion on the surface and edges of the ultrathin unit sheets. The holes generated in the layered photocatalysts only need to diffuse a very short (sub-nanometer) distance before reaching the surface of the unit sheets, where they can be trapped by interlayer water molecules. This rapid hole-trapping process allows electrons to freely and sufficiently diffuse within unit sheets until reaching the sheet edges [16]. Moreover, bismuth (Bi) is a kind of p-block metal with a d^{10} configuration, and the Bi 6s can hybridize O 2p levels to form a preferable hybridized valence band (VB), which favors the mobility of photogenerated holes in the VB and benefits the enhancement of the photocatalytic performance of the Aurivillius oxide semiconductors [17].

$Bi_4Ti_3O_{12}$ as a typical Aurivillius oxide (when $n = 3$) has been explored as a VLD photocatalyst since the discovery of photocatalytic behavior in the degradation of organic pollutants and water splitting. For instance, $Bi_4Ti_3O_{12}$ particulates, $Bi_4Ti_3O_{12}$ films and $Bi_4Ti_3O_{12}$ platelets have been reported as visible-light-driven photocatalysts [18–20]. Regrettably, the overall photocatalytic efficiency of individual phase $Bi_4Ti_3O_{12}$ nanomaterials is low because of the rapid recombination of electron–hole pairs after excitation. As we all know, compared to one individual semiconductor photocatalyst, hybrid photocatalysts integrate the synergistic effects

of the individual species, which can endow the composite systems with increased light harvesting, prolonged lifetime of carriers, enhanced catalytic performance as well as higher chemical stability [21]. Therein, $Bi_4Ti_3O_{12}$ based heterostructures such as $Bi_4Ti_3O_{12}/TiO_2$, $Bi_4Ti_3O_{12}/CuFe_2O_4$, and $Bi_4Ti_3O_{12}/BiOI$ have been reported [22–24]. Inspired by the above $Bi_4Ti_3O_{12}$/semiconductor systems, the construction of $Bi_4Ti_3O_{12}/Bi_2XO_6$ (X = Mo, W) heterostructure attracts our interest in particular because of their structural analogy. That is, both Bi_2MoO_6 and Bi_2WO_6 like $Bi_4Ti_3O_{12}$ belong to the same layered Aurivillius oxide family (the simplest member, when $n = 1$), with strong absorption in the visible light region. Bi_2XO_6 (X = Mo, W) and $Bi_4Ti_3O_{12}$ all consisting of $[Bi_2O_2]^{2+}$ layers (X–Bi–O–Bi–X) sandwiched between two slabs of X ions, atoms or groups (where X = $Bi_2Ti_3O_{10}{}^{2-}$, $MoO_4{}^{2-}$ or $WO_4{}^{2-}$). They can easily grow together to form heterostructures through ion exchange process [25]. Additionally, the conduction band (CB) of Bi_2XO_6 is lower or higher than that of $Bi_4Ti_3O_{12}$, the valence band (VB) of Bi_2XO_6 is also lower or higher than that of $Bi_4Ti_3O_{12}$. As a consequence, in the $Bi_4Ti_3O_{12}/Bi_2XO_6$ heterostructure, the interface between $Bi_4Ti_3O_{12}$ and Bi_2XO_6 is a "type II heterojunction", meaning that the valence band (VB) of $Bi_4Ti_3O_{12}$ is positioned (energetically) between the VB and CB of Bi_2XO_6, and the CB of $Bi_4Ti_3O_{12}$ is positioned above the VB and CB of Bi_2XO_6. When both $Bi_4Ti_3O_{12}$ and Bi_2XO_6 are activated simultaneously, the practical implication of this "staggered" configuration of energy levels is that the CB of Bi_2XO_6 acts as a sink of photogenerated electrons. Since the photogenerated holes move in the opposite direction, they accumulate in the VB of $Bi_4Ti_3O_{12}$, and thereby hinder charge recombination and improve photocatalytic efficiency.

Besides, many works show that the electrospun semiconductor metal oxide nanofiber photocatalyst is far more efficient than its nanoparticle analog in photocatalytic process, which attributed to efficient charge separation through interparticle charge transfer along the nanofiber framework [26,27]. Moreover, the electrospun nanofibers with both high porosity and large surface area being available for reaction are promising materials for surface modification and functionalization. Based on the above considerations, in this work we report a successful attempt for the fabrication of the $Bi_4Ti_3O_{12}/Bi_2XO_6$ (X = Mo, W) hierarchical heterostructures *via* a simple electrospinning technique and solvothermal method. It was found that the $Bi_4Ti_3O_{12}/Bi_2XO_6$ (X = Mo, W) hierarchical heterostructures exhibit excellent photocatalytic activity superior to the bare $Bi_4Ti_3O_{12}$ and Bi_2XO_6, which could be ascribed to the formation of the heterojunction, high specific surface area and hierarchical heterostructures. Moreover, due to the large length to diameter ratio, the as-electrospun nanofibers can be reclaimed easily by sedimentation without a decrease of the photocatalytic activity.

2. Experimental

2.1. Preparation of the $Bi_4Ti_3O_{12}$ nanofibers

For the preparation of $Bi_4Ti_3O_{12}$ nanofibers, 1.5 g of $Bi(NO_3)_3 \cdot 5H_2O$ and 0.8 g of $Ti(OC_4H_9)_4$ (TBT) were dissolved into 20 mL N,N-dimethylformamide (DMF). When the mixture stirring to dissolve, it was slowly added into 2.5 g of polyvinylpyrrolidone (PVP, Mw = 1,300,000), followed by magnetic stirring at room temperature for overnight (with the solution held in a capped bottle). The solution was transferred into a plastic syringe equipped with a capillary. A copper pin connected to a high-voltage generator was placed in the solution, and the solution was kept in the capillary by adjusting the angle between capillary and the fixing support. A square metal plate, covered with an aluminum foil was employed as the collector. A voltage of 7.5 kV was applied to the solution. The

composite fibers of $Bi(NO_3)_3$–TBT–PVP dried initially 2 h at 90 °C under vacuum, and then calcined in the air at 600 °C at a rising rate of 30 °C/h and remained at the required temperature for 2 h. The as-obtained $Bi_4Ti_3O_{12}$ nanofibers were denoted by BTO.

2.2. Fabrication of $Bi_4Ti_3O_{12}/Bi_2XO_6$ (X = Mo, W) hierarchical heterostructures

0.1 mmol $Bi(NO_3)_3 \cdot 5H_2O$ and 0.1 mmol $Na_2XO_4 \cdot 2H_2O$ (X = Mo, W) were dissolved in 5 mL of ethylene glycol (EG) under magnetic stirring, respectively. The two solutions were mixed together, and then 30 mL ethanol was added into the above solution, followed by stirring for 5 min. The resulting clear solution and $Bi_4Ti_3O_{12}$ nanofibers (15 mg) were transferred into a 50 mL Teflon-lined stainless steel autoclave, which was heated to 160 °C and maintained for 24 h. Then, the autoclave was cooled down to room temperature. The obtained composite materials were washed with ethanol to remove any ionic residual. Then the materials dried in an oven at 90 °C for 2 h. The as-fabricated $Bi_4Ti_3O_{12}/Bi_2XO_6$ (X = Mo, W) heterocatalysts were denoted by BTO/BXO (X = Mo, W). For comparison, Bi_2MoO_6 and Bi_2WO_6 powder were synthesized in the absence of $Bi_4Ti_3O_{12}$ nanofibers.

2.3. Photocatalytic test

In all photocatalytic activity of experiments, the samples (0.05 g) were put into a solution of RB dye (50 mL, 10 ppm), which was irradiated with a 300 W Xe lamp equipped with an ultraviolet cut-off filter to provide visible light with $\lambda \geq 400$ nm. The catalytic reaction was conducted at room temperature. Decreases in the concentrations of dyes were analyzed by a UV–vis–NIR spectrophotometer (Perkin-Elmer, Lambda 850) at $\lambda = 554$ nm. At given intervals of illumination, the samples (3 mL) of the reaction solution were taken out and then centrifuged and filtered. Finally, the filtrates were analyzed.

2.4. Characterization

The morphology and the crystal structure of the synthesized materials were characterized by field-emission scanning electron microscopy (FE-SEM; SU70, Hitachi, Japan), transmission electron microscopy (TEM; FEI, Tecnai TF20) and X-ray diffraction (XRD; D/max2600, Rigaku, Japan). An energy dispersive X-ray (EDX) spectroscope coupled to a FE-SEM was used to analyze the composition of the samples. X-ray photoelectron spectroscopy (XPS) which was K-alpha X-ray spectrometer (Thermofisher Scientific Company) with Al source, the standard binding energy of C 1s is 285 eV. The specific surface areas of the samples were measured with a Micromeritics ASAP 2010 instrument and analyzed by the Brunauer–Emmett–Teller (BET) method. UV–vis diffuse reflectance spectra (DRS) of the samples are obtained by using a UV–vis spectrometer (Perkin–Elmer, Lambda 850) used polytetrafluoroethylene (PTFE) as a reference and is converted to absorbance by the Kubelka–Munk method.

The photocurrent was conducted by using an electrochemical analyzer (CHI660E, ChenHua Instruments, Shanghai, China) with a standard three-electrode configuration, which employed a Pt wire as a counter electrode, a saturated calomel electrode as a reference electrode and fluorine-doped tin oxide (FTO) as working electrode. 10 mg of sample powder was dispersed into 2 mL of N,N-dimethylformamide under ultrasonication for 10 min to obtain slurries. The as-prepared slurries were spread onto the surface of FTO glasses to obtain sample films with the region of 1 cm × 1 cm. These as-prepared FTO glass electrodes were dried at 100 °C for 60 min under ambient conditions to improve adhesion. 50 mL of 0.5 M Na_2SO_4 (pH 6.8) was used as the electrolyte solution. A 300 W
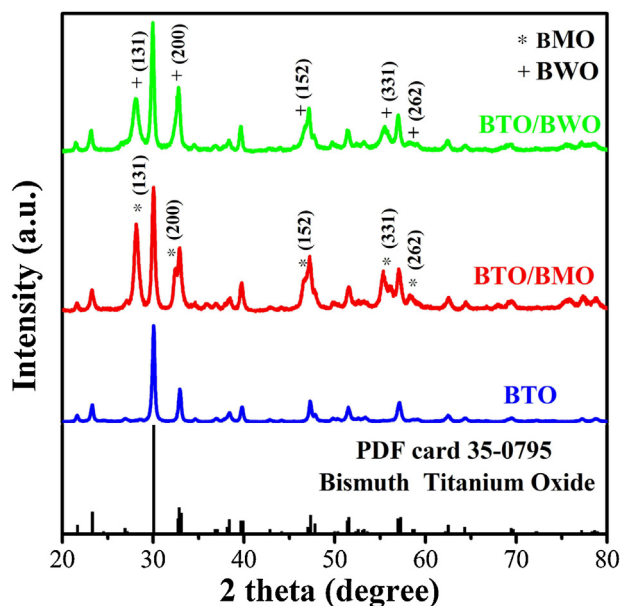
Fig. 1. XRD patterns of samples (BTO, BTO/BMO and BTO/BWO).

xenon lamp with a 420 nm cut-off filter was employed as a visible light photosource.

3. Results and discussions

Fig. 1 shows the XRD pattern of the $Bi_4Ti_3O_{12}$ nanofibers and $Bi_4Ti_3O_{12}/Bi_2XO_6$ (X = Mo, W) hierarchical heterostructures. As shown in Fig. 1, the diffraction peaks of the BTO nanofibers can be indexed to the pure orthorhombic $Bi_4Ti_3O_{12}$ (JCPDS no. 35-0795). No peaks of impurities can be observed, demonstrating the high phase purity of the as-prepared $Bi_4Ti_3O_{12}$ nanofibers. As for the BTO/BXO (X = Mo, W) heterostructures, except the diffraction peaks of $Bi_4Ti_3O_{12}$, the diffraction peaks of the Bi_2MoO_6 and Bi_2WO_6 with 2θ values of 28.3°, 32.5° (Bi_2WO_6, 32.8°), 46.4°, 55.4° (Bi_2WO_6, 55.8°), 58.5° are also clearly observed corresponding to (1 3 1), (2 0 0), (1 5 2), (3 3 1) and (2 6 2) crystal planes of koechlinite Bi_2MoO_6 (JCPDS no.21-0102) and russellite Bi_2WO_6 (JCPDS no.39-0256). These results suggest that the Bi_2MoO_6 and Bi_2WO_6 have been formed on the $Bi_4Ti_3O_{12}$ nanofibers by solvothermal processing.

Typical SEM images of the $Bi_4Ti_3O_{12}$ nanofibers and $Bi_4Ti_3O_{12}/Bi_2XO_6$ (X = Mo, W) hierarchical heterostructures are shown in Fig. 2. It can be clearly seen that all these samples possess a regular one-dimensional morphology. Fig. 2a shows the SEM image of $Bi(NO_3)_3$–TBT–PVP nanofibers which are fabricated by electrospinning. It can be clearly seen that the nanofibers are of a relatively smooth surface with a diameter around 150 nm. Fig. 2b displays the SEM images for the products that are obtained by annealing the as-spun $Bi(NO_3)_3$–TBT–PVP nanofibers at 600 °C. Obviously, the $Bi_4Ti_3O_{12}$ nanofibers with a lot of pores are formed and the diameters reduce to an average diameter of 80 nm compared to the as-spun nanofibers, resulting from the decomposition of $Bi(NO_3)_3$, TBT and PVP. Fig. 2c and d shows the SEM images of $Bi_4Ti_3O_{12}/Bi_2MoO_6$ and $Bi_4Ti_3O_{12}/Bi_2WO_6$ hierarchical heterostructures, respectively. As shown in the inset of Fig. 2c and d, a lot of Bi_2MoO_6 or Bi_2WO_6 nanosheets grew on the surface of $Bi_4Ti_3O_{12}$ nanofibers after solvothermal reaction. The nanosheets appeared to distribute uniformly. It can be seen from the high magnification SEM image that the nanosheets are in fact very thin flakes with an average thickness of about 30 nm and an average edge length of about 60–80 nm.

To clarify the composition distribution of the product and structure properties, the spatial distribution of the compositional elements within the heterostructures is obtained by using SEM–EDX line scans along the nanofiber's radial direction (marked by the yellow line in the inset to Fig. 3a and b). There are three signal peaks in Bi, Ti, and Mo or W, as shown in Fig. 3a and b. The Ti signal is mainly confined within the $Bi_4Ti_3O_{12}$ core area, while a higher intensity of Mo or W is found in the shell region. Bi signal appears within the core and the shell. This is consistent with the $Bi_4Ti_3O_{12}$ core–Bi_2XO_6 (X = Mo, W) shell nanofiber configuration observed in the SEM image. In addition, EDX analysis indicates that the molar ratio of Bi_2MoO_6 and $Bi_4Ti_3O_{12}$ is about 5:6 for $Bi_4Ti_3O_{12}/Bi_2MoO_6$ heterostructures, and the molar ratio of Bi_2WO_6 and $Bi_4Ti_3O_{12}$ is about 2:1 for $Bi_4Ti_3O_{12}/Bi_2WO_6$ heterostructures.

The $Bi_4Ti_3O_{12}/Bi_2XO_6$ (X = Mo, W) hierarchical heterostructures are further examined using transmission electron microscopy (TEM). Fig. 4a and c shows the typical TEM images of $Bi_4Ti_3O_{12}/Bi_2MoO_6$ and $Bi_4Ti_3O_{12}/Bi_2WO_6$ hierarchical heterostructures. The TEM images reveal that highly dense secondary Bi_2MoO_6 and Bi_2WO_6 nanosheets are uniformly coated around the primary $Bi_4Ti_3O_{12}$ nanofiber substrates, coinciding with the results from the SEM observations. We expect that these Bi_2MoO_6 nanosheets possess relatively high surface areas due to their small size and two-dimensional morphologies. The high surface areas are very beneficial in catalyst design since it can facilitate the molecular transport of reactants and products. The HRTEM image from two hierarchical heterostructures all displayed two types of clear lattice fringes as shown in Fig. 4b and d, respectively. The fringe observed in Fig. 4b corresponds to the interplanar distance of 0.38 nm, which agreed well with the lattice spacing of the (1 1 1) plane of the $Bi_4Ti_3O_{12}$. In addition, another set of fringes spaced at 0.27 nm corresponded to the (2 0 0) lattice spacing of Bi_2MoO_6. The fringe observed in Fig. 4d corresponds to the interplanar distance of 0.33 nm, which agreed well with the lattice spacing of the (1 5 1) plane of the $Bi_4Ti_3O_{12}$. Another set of fringes spaced at 0.31 nm corresponds to the (1 3 1) lattice spacing of Bi_2WO_6. The HRTEM images clearly exhibit that the as-adopted fabrication route is successful to realize a close contact of Bi_2XO_6 (X = Mo, W) nanosheets with $Bi_4Ti_3O_{12}$ nanoparticles in the $Bi_4Ti_3O_{12}/Bi_2XO_6$ (X = Mo, W) hierarchical heterostructures. Such a close contact is very beneficial to the separation of photogenerated electron–hole pairs in the process of photocatalytic reaction.

The chemical composition and purity of the $Bi_4Ti_3O_{12}/Bi_2XO_6$ (X = Mo, W) hierarchical heterostructures are studied by XPS analysis. The fully scanned spectra (Fig. 5a) demonstrate that Bi, Ti, O, and C elements exist in bare $Bi_4Ti_3O_{12}$ nanofibers, while Bi, Ti, Mo, O, and C exist in $Bi_4Ti_3O_{12}/Bi_2MoO_6$ hierarchical heterostructures, and Bi, Ti, W, O, and C exist in $Bi_4Ti_3O_{12}/Bi_2WO_6$ hierarchical heterostructures, respectively. Fig. 5b shows that the Bi $4f_{7/2}$ and Bi $4f_{5/2}$ peaks of $Bi_4Ti_3O_{12}/Bi_2WO_6$ locate at 159 and 164.4 eV, while the Bi $4f_{7/2}$ and Bi $4f_{5/2}$ peaks of $Bi_4Ti_3O_{12}/Bi_2MoO_6$ locate at 158.8 and 164.2 eV, respectively [28]. The Bi $4f_{7/2}$ and Bi $4f_{5/2}$ peaks of metallic bismuth locate at 156.8 and 162.2 eV through the previous literatures. However, the chemical shift of the Bi 4f and metallic Bi is 2.2 eV and 2.0 eV respectively, which is less than the typical value of 3.1 eV between Bi_2O_3 and metallic Bi [29,30]. It illustrates the valence state of bismuth is (+3 – x), due to a lack of oxygen and an enhanced concentration of oxygen vacancies near the bismuth ions, which are more likely inside the Bi_2O_2 layer [31]. The oxygen vacancy has been proven to have a vital role in the electronic structures and physical properties of oxide materials. The oxygen vacancy serving as electron traps can enhance the efficiency of visible light absorption [32–34]. In addition, the XPS peaks of $Bi_4Ti_3O_{12}/Bi_2MoO_6$ at 232 eV and 235 eV are assigned to Mo $3d_{5/2}$ and Mo $3d_{3/2}$, respectively (Fig. 5c). The XPS peaks of

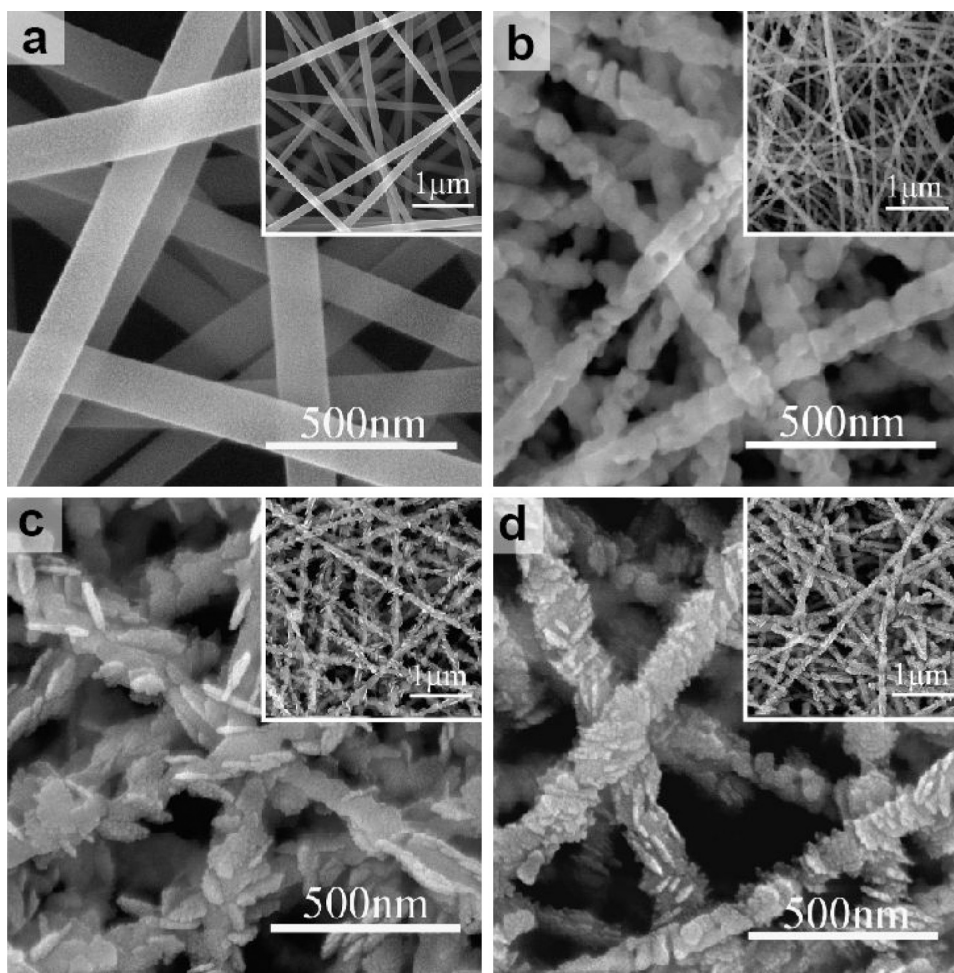**Fig. 2.** SEM images of the samples. (a) Bi(NO$_3$)$_3$–TBT–PVP nanofibers; (b) BTO; (c) BTO/BMO; (d) BTO/BWO.

Bi$_4$Ti$_3$O$_{12}$/Bi$_2$WO$_6$ at 34.4 eV and 37.6 eV are assigned to W 4f$_{7/2}$ and W 4f$_{5/2}$, respectively (Fig. 5d).

Fig. 6 shows nitrogen adsorption–desorption isotherms of Bi$_4$Ti$_3$O$_{12}$ nanofibers and Bi$_4$Ti$_3$O$_{12}$/Bi$_2$XO$_6$ (X = Mo, W) hierarchical heterostructures and corresponding pore size distribution curves. The specific surface area of the samples, calculated by the multipoint Brunauer–Emmett–Teller (BET) method, are 10.876 m^2/g for Bi$_4$Ti$_3$O$_{12}$ nanofibers, 27.938 m^2/g for Bi$_4$Ti$_3$O$_{12}$/Bi$_2$MoO$_6$ heterostructures and 29.435 m^2/g for Bi$_4$Ti$_3$O$_{12}$/Bi$_2$WO$_6$ heterostructures. The corresponding pore size distribution curve is obtained by the BJH method, and indicated a relatively narrow pore size distribution centered at about 3–6 nm (Fig. 6b). The high surface area and small pore allow not only more surface to be reached by the incident light but also more active catalytic sites, which results in the good photocatalytic performance.
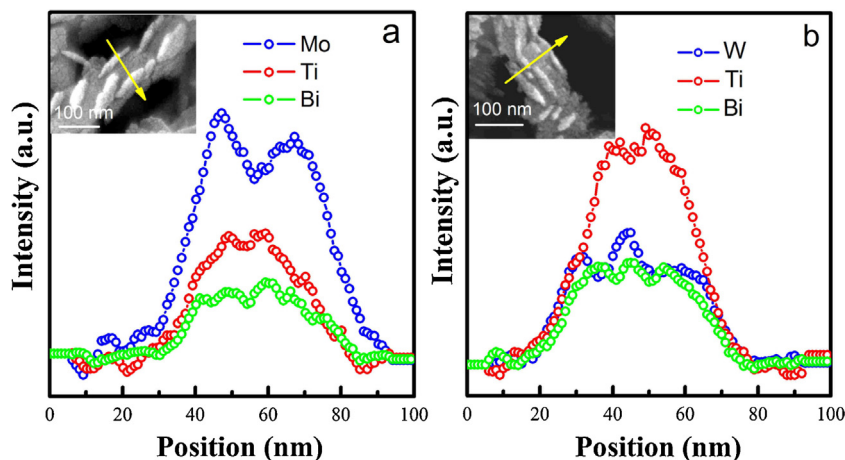

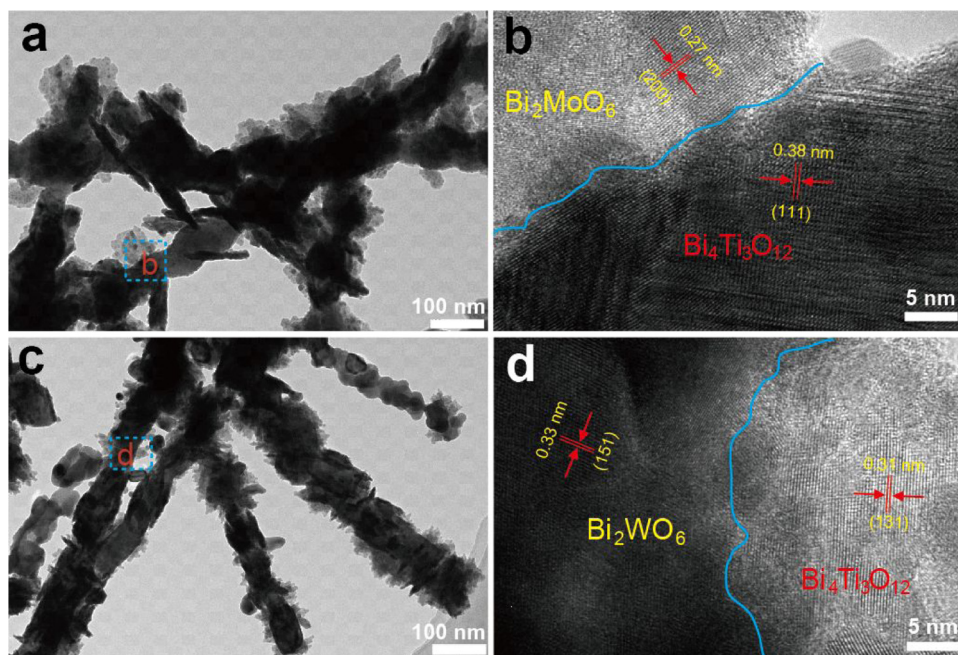**Fig. 3.** SEM–EDX line scans spectra of samples. (a) BTO/BMO; (b) BTO/BWO.

Fig. 4. (a, c) TEM images of the sample BTO/BXO (X = Mo or W); (b, d) HRTEM images of the heterojunction region.
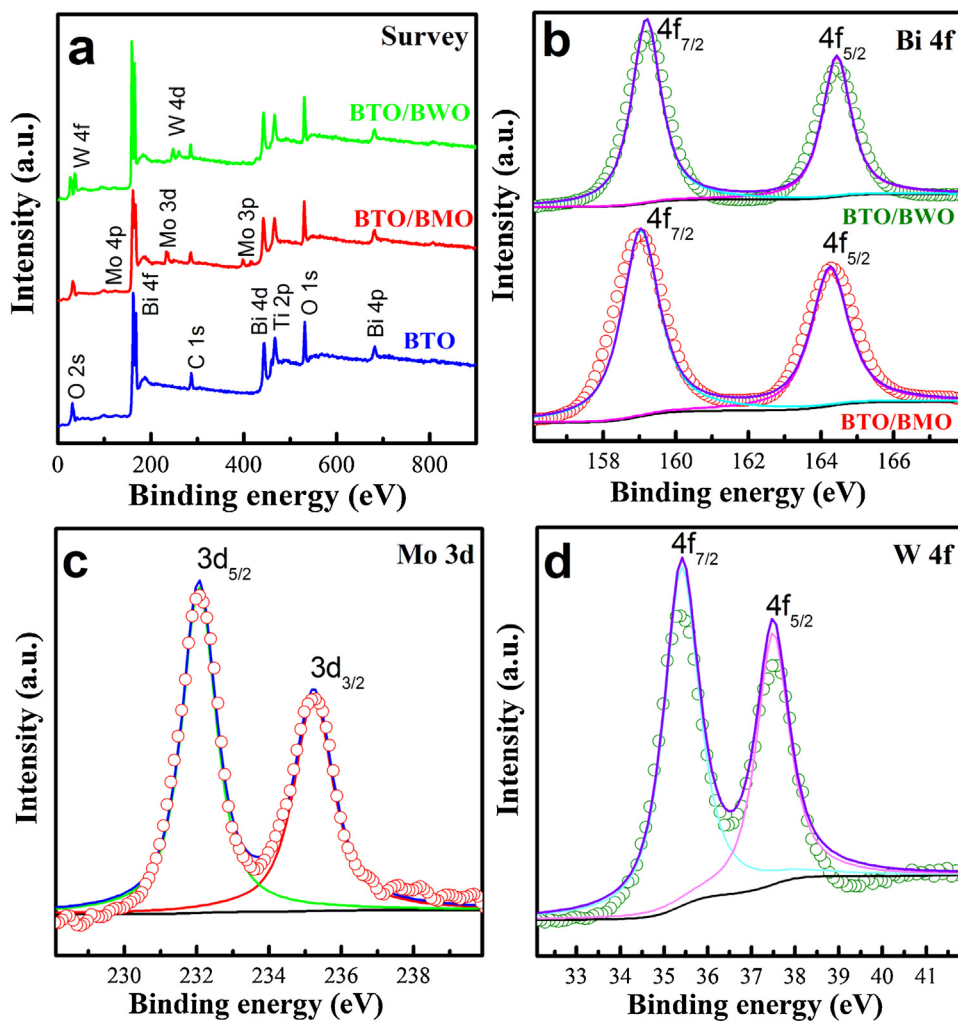

Fig. 5. (a) Survey XPS spectrum of BTO, BTO/BMO and BTO/BWO; high-resolution XPS spectra of (b) Bi 4f, (c) Mo 3d and (d) W 4f.
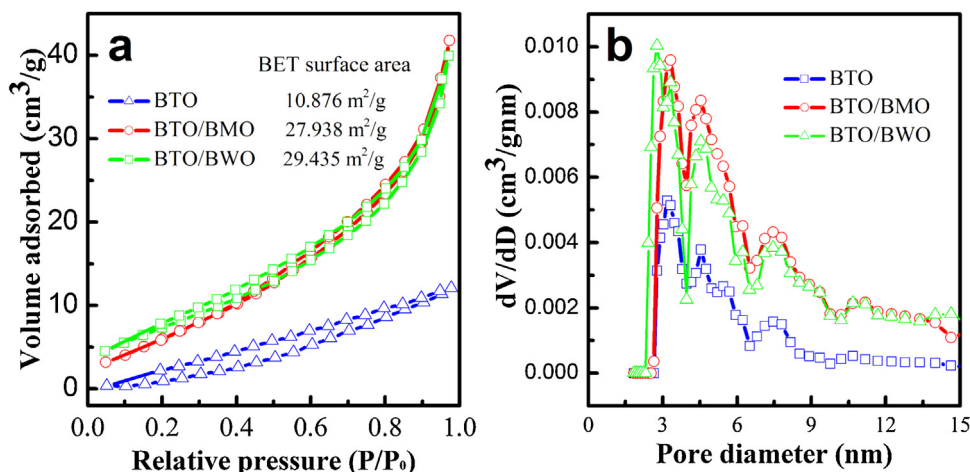
Fig. 6. N$_2$ absorption–desorption isotherm (a) and pore–size distribution curves (b) of the samples BTO and BTO/BXO (X = Mo or W).

The UV–vis diffuse reflectance spectra in the wavelength range of 200–600 nm for the Bi$_4$Ti$_3$O$_{12}$ nanofibers and Bi$_4$Ti$_3$O$_{12}$/Bi$_2$XO$_6$ (X = Mo, W) hierarchical heterostructures are shown in Fig. 7. For a crystalline semiconductor, the optical absorption near the band edge follows the equation $\alpha(h\nu) = A(h\nu - E_g)^{n/2}$, where α, ν, A and E_g are the absorption coefficient, light frequency, a constant and band gap energy, while n depends on the characteristic of the transition in a semiconductor. For Bi$_4$Ti$_3$O$_{12}$, the value of n is 4 for the indirect transition. The band gap of the pure Bi$_4$Ti$_3$O$_{12}$ nanofibers is estimated to be 2.87 eV. For the Bi$_4$Ti$_3$O$_{12}$/Bi$_2$MoO$_6$ and Bi$_4$Ti$_3$O$_{12}$/Bi$_2$WO$_6$ hierarchical heterostructures, the absorbance spectra show red shift of the absorption edge. The extending of absorption edges possibly led to better photocatalytic efficiency, especially under visible light irradiation.

The photocatalytic activity of the Bi$_4$Ti$_3$O$_{12}$/Bi$_2$XO$_6$ (X = Mo, W) hierarchical heterostructures is evaluated by the decomposition of rhodamine B (RB) under visible light irradiation. Temporal changes in the concentration of RB, as monitored by the maximal absorption of RB at 554 nm in the UV–vis spectra over the as-prepared photocatalysts, are shown in Fig. 8. The degradation efficiency of all the samples is defined as C/C_0, where C and C_0 represent the remnant and initial concentrations of RB, respectively. For comparison, Degussa-P25, physical mixture Bi$_2$XO$_6$

and Bi$_4$Ti$_3$O$_{12}$ samples are used as the photocatalytic reference to understand the photocatalytic activity of the above hierarchical nanostructures (molar ratios of Bi$_4$Ti$_3$O$_{12}$ and Bi$_2$XO$_6$ are the same as corresponding Bi$_4$Ti$_3$O$_{12}$/Bi$_2$XO$_6$ hierarchical heterostructures). As observed in Fig. 8a, there is no appreciable degradation of the above organic dyes after 90 min in the absence of photocatalysts. And, Degussa-P25 has very weak photocatalytic activity under visible light irradiation, except the decent adsorption for RB, which can be attributed to the high specific surface area and photosensitization from RB molecule. It can be seen that physical mixture Bi$_4$Ti$_3$O$_{12}$ + Bi$_2$MoO$_6$ and Bi$_4$Ti$_3$O$_{12}$ + Bi$_2$WO$_6$ samples exhibit negligible activity and the photodegradation efficiency of RB reached about 64% and 27% after 90 min of reaction, respectively. In comparison, 97% and 91% of RB is photocatalytically degraded by Bi$_4$Ti$_3$O$_{12}$/Bi$_2$MoO$_6$ and Bi$_4$Ti$_3$O$_{12}$/Bi$_2$WO$_6$ hierarchical heterostructures within 90 min under visible light irradiation, which demonstrates that the Bi$_4$Ti$_3$O$_{12}$/Bi$_2$XO$_6$ hierarchical heterostructures exhibit an enhanced visible-light-driven photocatalytic performance. The photodegradation reaction can be described by first-order kinetics with respect to the concentration of the organic compound. The time-dependent decomposition of RB follows the first-order kinetics, $\ln C_0/C = kKt = k_{app}t$, where t is the irradiation time and k is the rate constant. The calculated curves of k for the reaction in the presence of Bi$_4$Ti$_3$O$_{12}$/Bi$_2$MoO$_6$, Bi$_4$Ti$_3$O$_{12}$/Bi$_2$WO$_6$, Bi$_4$Ti$_3$O$_{12}$ + Bi$_2$MoO$_6$, Bi$_4$Ti$_3$O$_{12}$ + Bi$_2$WO$_6$ and P25 are 0.0378, 0.0244, 0.0112, 0.0032 and 0.0017 min^{-1}, respectively, as shown in Fig. 8b, which is well-consistent with the activity studies above.

The enhanced photocatalytic performance of Bi$_4$Ti$_3$O$_{12}$/Bi$_2$XO$_6$ (X = Mo, W) hierarchical heterostructures is due to the following factors: firstly, the BET surface area of the Bi$_4$Ti$_3$O$_{12}$/Bi$_2$MoO$_6$ and Bi$_4$Ti$_3$O$_{12}$/Bi$_2$WO$_6$ is estimated to be about 29.435 and 27.938 m^2/g, which is much higher than that of the Bi$_4$Ti$_3$O$_{12}$ nanofibers (10.876 m^2/g). The large surface area for the heterostructure allows not only more surface to be irradiated by the incident light but also more active photocatalytic sites, which results in excellent photocatalytic activity. Secondly, the higher photocatalytic activity of the Bi$_4$Ti$_3$O$_{12}$/Bi$_2$XO$_6$ (X = Mo, W) hierarchical heterostructures can also be ascribed to the 1D nanostructures. It has been reported that high-quality 1D nanostructured semiconductors have been considered as model systems for efficient transport of electrons and optical excitations [26,27]. Thirdly, we believe that the Bi$_2$XO$_6$ nanosheets with an reflections of electromagnetic waves, such as ultraviolet and visible light, thus allowing more efficient use of the light source and therefore endowing these hierarchical heterostructure fabrics with greatly enhanced visible light
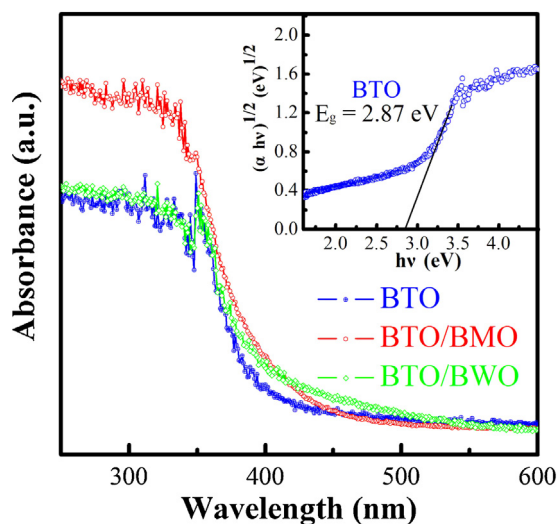

Fig. 7. UV–vis diffuse reflectance spectra of (a) BTO, (b) BTO/BMO, and (c) BTO/BWO.
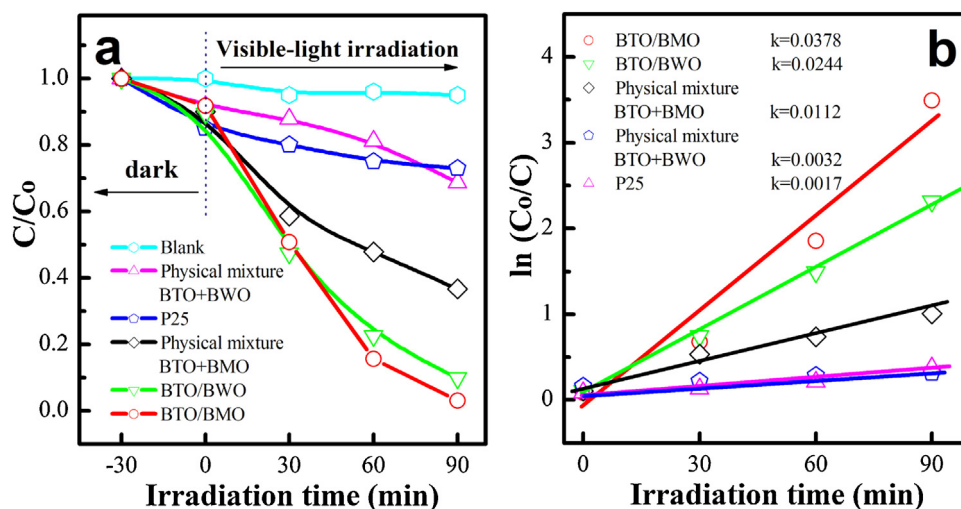
Fig. 8. (a) Degradation curves of RB over different catalyst under visible light. (b) Kinetic linear simulation curves of RB photocatalytic degradation with different photocatalysts.

photocatalytic properties. Last but not least, the presence of heterojunction in the $Bi_4Ti_3O_{12}/Bi_2XO_6$ (X = Mo, W) heterostructures also improves the composite activity, which favored the separation of photogenerated electron–hole pairs in the heterostructures. In this work, the as-adopted preparation process is successful to realize a close contact of Bi_2MoO_6 or Bi_2WO_6 nanosheets with $Bi_4Ti_3O_{12}$ nanoparticles in $Bi_4Ti_3O_{12}/Bi_2XO_6$ (X = Mo, W) heterostructures, as proved by SEM and HRTEM observations above. Such a close contact is more effective in the inhibition of the photogenerated electron–hole recombination. The heterojunction effect can only occur on closely contacted interfaces within the heterostructures. Indeed, enhanced photocatalytic activity is observed for the synthesized $Bi_4Ti_3O_{12}/Bi_2XO_6$ (X = Mo, W) heterojunction than for the mechanically mixed $Bi_4Ti_3O_{12}$ and Bi_2XO_6 (X = Mo, W) samples with same molar ratios, because the latter only has more loosely contacted interfaces.

It is interesting to investigate the plausible photocatalytic mechanism for the superior photocatalytic activity of $Bi_4Ti_3O_{12}/Bi_2XO_6$ heterostructure. A possible charge transfer mechanism of the $Bi_4Ti_3O_{12}/Bi_2XO_6$ heterostructure is proposed and illustrated in Scheme 1. As shown in Scheme 1, all components in the heterojunction with band gap energy (2.87 eV for $Bi_4Ti_3O_{12}$, 2.68 eV for Bi_2MoO_6 and 2.82 eV for Bi_2WO_6) can be easily excited by visible light and induce the generation of photoelectrons and holes. The conduction band (CB) edges of $Bi_4Ti_3O_{12}$, Bi_2MoO_6 and Bi_2WO_6 are
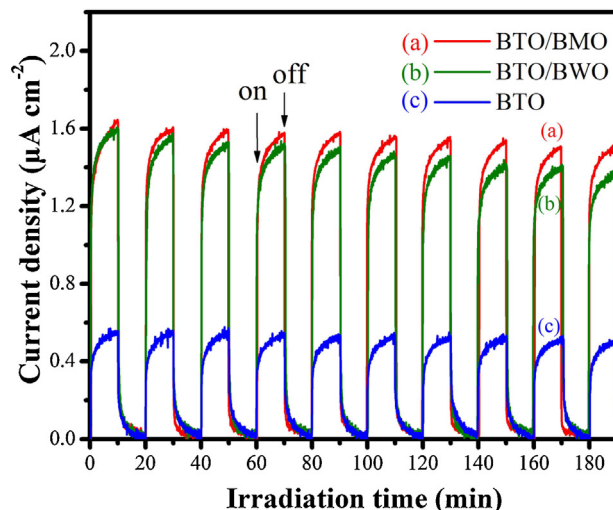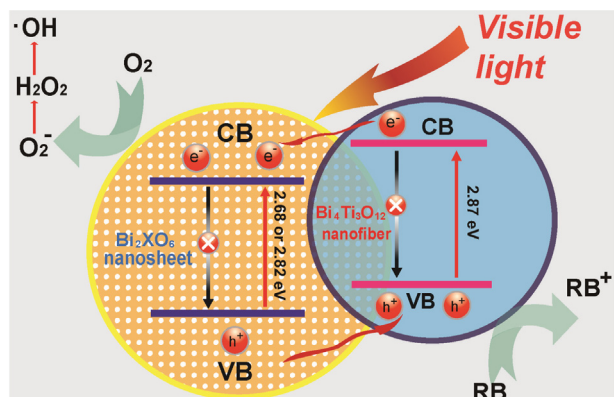

Fig. 9. Transient photocurrent responses of the samples: (a) BTO, (b) BTO/BMO, and (c) BTO/BWO.

Scheme 1. Schematic of the band structures of $Bi_4Ti_3O_{12}/Bi_2XO_6$ (X = Mo or W) heterostructures and possible electron–hole separations.
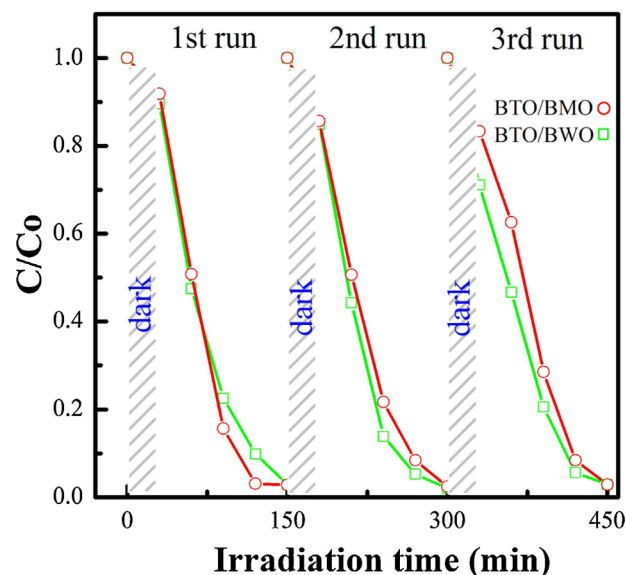

Fig. 10. Degradation curves of RB over sample BTO/BXO (X = Mo or W) for reusing three times.
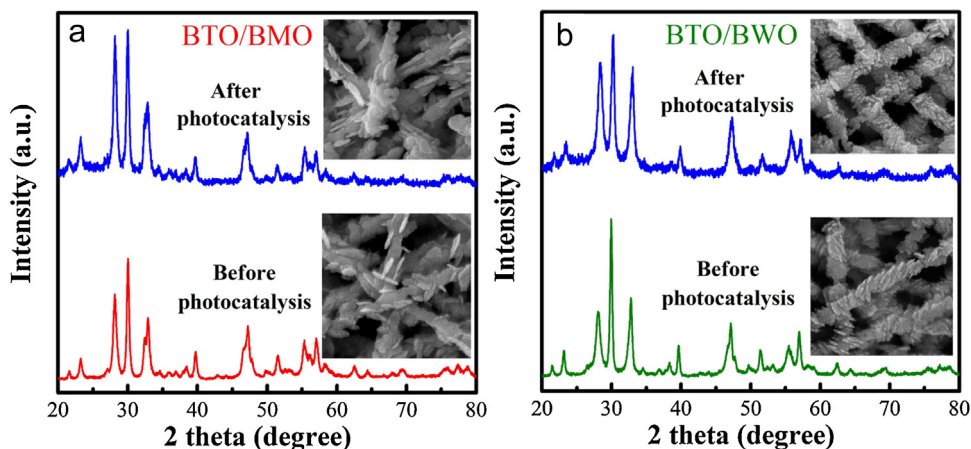
Fig. 11. XRD patterns and SEM images of sample BTO/BMO (a) and BTO/BMO (b) photocatalyst before and after three times photocatalytic reaction.

0.05 eV, −0.32 eV and 0.24 eV [23,35]. The corresponding valence band (VB) edges were 2.92 eV, 2.36 eV and 3.2 eV respectively. When $Bi_4Ti_3O_{12}$ and Bi_2XO_6 (X = Mo, W) are coupled, a type II heterojunction is formed in the staggered arrangement at the $Bi_4Ti_3O_{12}/Bi_2XO_6$ (X = Mo, W) interface. From Scheme 1, the conduction band of the Bi_2XO_6 (X = Mo, W) is positive than that of the $Bi_4Ti_3O_{12}$ and the valence band of the $Bi_4Ti_3O_{12}$ is negative than that of the Bi_2XO_6 (X = Mo, W). When the $Bi_4Ti_3O_{12}/Bi_2XO_6$ (X = Mo, W) are excited by visible light, the photogenerated electrons in the $Bi_4Ti_3O_{12}$ transfer from the conduction band of $Bi_4Ti_3O_{12}$ to the Bi_2XO_6 (X = Mo, W) due to the lower conduction band level of Bi_2XO_6 (X = Mo, W), meanwhile, the photogenerated holes in the Bi_2XO_6 (X = Mo, W) transfer from the Bi_2XO_6 (X = Mo, W) to $Bi_4Ti_3O_{12}$ because of the higher valence level of $Bi_4Ti_3O_{12}$. Thus, photogenerated electrons and holes are spatially separated from each other, reducing the recombination probability significantly and increasing electron lifetimes.

The better separation of electrons and holes in the $Bi_4Ti_3O_{12}/Bi_2XO_6$ is confirmed by the transient photocurrent responses (Fig. 9). $Bi_4Ti_3O_{12}/Bi_2XO_6$ heterostructure exhibited an increased current density, about three times than that of the bare $Bi_4Ti_3O_{12}$. The increased current density indicated an enhancing photoinduced electrons and holes separation efficiency. These well-separated photoelectrons and holes would further degrade dye molecules. Meanwhile, the generated conduction band electrons (e^-) probably reacted with dissolved oxygen molecules to yield superoxide radical anions, O_2^-, which on protonation generated the hydroperoxy, $HO_2^\bullet$, radicals, producing hydroxyl radical $OH^\bullet$, which was a strong oxidizing agent to decompose the organic dye. Since the $Bi_4Ti_3O_{12}$ (h^+) radicals could oxidize a suitable
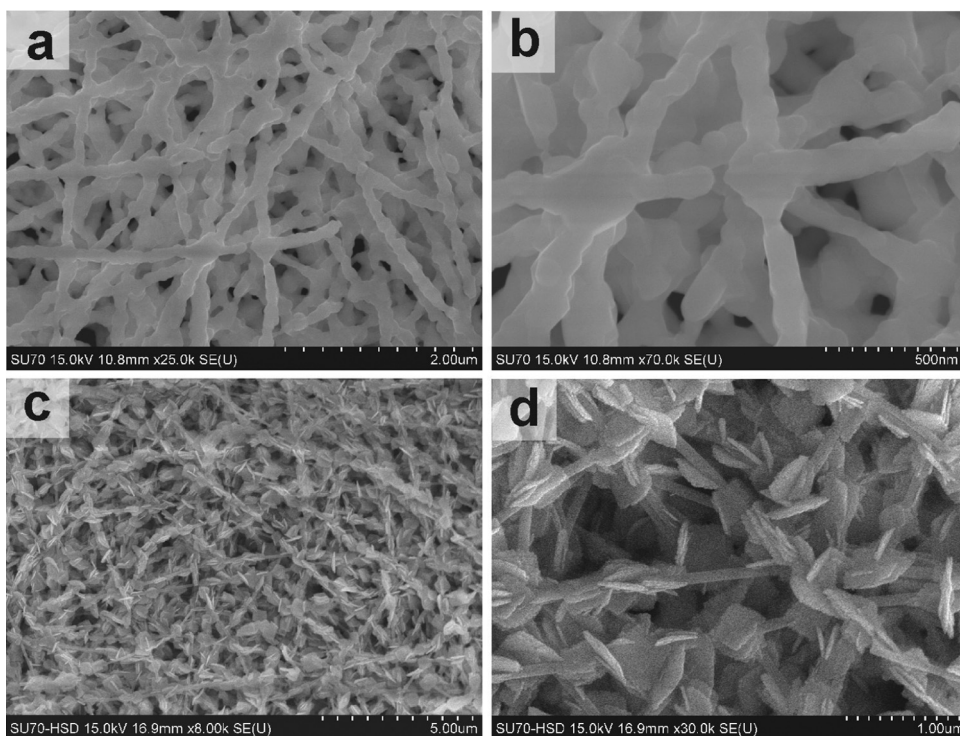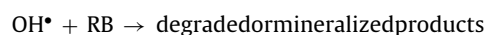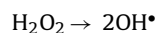

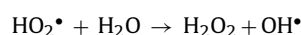**Fig. 12.** SEM images of $Bi_4Ti_3O_{12}/BiVO_4$ (a, b) and $Bi_4Ti_3O_{12}/BiOCl$ (c, d) heterostructures.

substrate (R), together with recovery of the original $Bi_4Ti_3O_{12}$. The hypothetical mechanism is proposed for the photocatalytic degradation of RB as follows:

$$Bi_4Ti_3O_{12} + h\nu \rightarrow Bi_4Ti_3O_{12}(e^- + h^+)$$

$$Bi_2XO_6 + h\nu \rightarrow Bi_2XO_6(e^- + h^+)$$

$$Bi_4Ti_3O_{12}(e^- + h^+) + Bi_2XO_6(e^- + h^+) \rightarrow Bi_2XO_6(2e^-)$$
$$+ Bi_4Ti_3O_{12}(2h^+)$$

$$Bi_2XO_6(e^-) + O_2 \rightarrow Bi_2XO_6 + O_2^-$$

$$O_2^- + H_2O \rightarrow HO_2^\bullet + OH^-$$

$$HO_2^\bullet + H_2O \rightarrow H_2O_2 + OH^\bullet$$

$$H_2O_2 \rightarrow 2OH^\bullet$$

$$OH^\bullet + RB \rightarrow degradedormineralizedproducts$$

$$Bi_4Ti_3O_{12}(h^+) + RB \rightarrow degradedormineralizedproducts$$
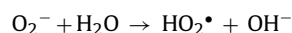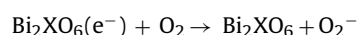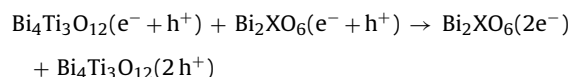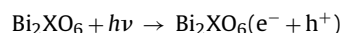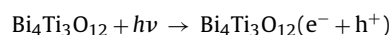
Recycling as well as maintaining a high photocatalytic activity is a critical issue for the long-term use of catalysts in practical applications. It is known that the photocorrosion or photodissolution of catalysts might occur on the photocatalyst surface in the photocatalytic reaction. To test the stability of $Bi_4Ti_3O_{12}/Bi_2XO_6$ (X = Mo, W) photocatalyst on RB photodegradation, we reuse the catalyst three times. As shown in Fig. 10, each experiment is carried out under identical conditions. After three cycles, the photocatalytic activity of the $Bi_4Ti_3O_{12}/Bi_2XO_6$ (X = Mo, W) remained almost unchanged. However, the adsorption property of $Bi_4Ti_3O_{12}/Bi_2XO_6$ (X = Mo, W) heterostructures improves significantly after three runs in the dark. According to the previous literature, some oxides exhibit photoinduced hydrophilicity [36,37]. Briefly, it has been found that these inorganic-oxide-based photoresponsive wettability transitions conform to a similar mechanism. The photoinduced redox processes of the oxide, the generation and annihilation of oxygen vacancies, the absorption of water molecules, and the presence of environmental gases have strong influences on the switching process. It is important to note that the surface of photocatalyst can revert to the original state after dark storage for a long period. In our work, the $Bi_4Ti_3O_{12}/Bi_2XO_6$ (X = Mo, W) heterostructures do not experience the dark recovery process after one or two runs. Therefore, the $Bi_4Ti_3O_{12}/Bi_2XO_6$ (X = Mo, W) heterostructures may be obtain some hydrophilic. The hydrophilic can facilitate more efficient contact of hierarchical $Bi_4Ti_3O_{12}/Bi_2XO_6$ (X = Mo, W) heterostructures with organic contaminants and thus improve its adsorption activity.

The morphologies and crystalline structures of $Bi_4Ti_3O_{12}/Bi_2XO_6$ (X = Mo, W) photocatalysts after three cycles are also studied. SEM images of $Bi_4Ti_3O_{12}/Bi_2XO_6$ (X = Mo, W) after three cycles show that the catalyst still has one-dimensional structure (Fig. 11). As shown in XRD patterns in Fig. 11, after three catalytic runs, the position and the ratio of peaks are nearly the same as that of fresh photocatalyst. No detachment or aggregation of $Bi_4Ti_3O_{12}/Bi_2XO_6$ (X = Mo, W) photocatalysts during the catalytic reaction is observed, indicating that the special heterostructures protect the Bi_2XO_6 (X = Mo, W) from being lost, resulting in the preservation of the excellent activity and structural stabilities during multiple recycles. Moreover, the $Bi_4Ti_3O_{12}/Bi_2XO_6$ (X = Mo, W) photocatalysts are of one-dimensional nanofiber morphology and can be easily separated from an aqueous suspension only by sedimentation.

The simple experimental procedure for the $Bi_4Ti_3O_{12}/Bi_2XO_6$ heterostructure makes this method quite simple, environmentally benign, and cost-effective for the synthesis of other heterostructures for various applications. Fig. 12 shows the SEM image of $Bi_4Ti_3O_{12}/BiVO_4$ and $Bi_4Ti_3O_{12}/BiOCl$ heterostructure prepared by the similar method. It can be seen that two examples of related bismuth oxides can be successfully fabricated, demonstrating the generality of the present method. We believe such method may open new pathways to designing other Aurivillius oxide heterostructure for potential applications. Our related work is in progress and will be published later.

4. Conclusion

In summary, by using solvothermal process and electrospinning technology, the $Bi_4Ti_3O_{12}/Bi_2XO_6$ (X = Mo, W) hierarchical heterostructures with novel architectures were successfully fabricated. In comparison to physical mixture $Bi_4Ti_3O_{12}$ and Bi_2XO_6 (X = Mo, W) samples, the $Bi_4Ti_3O_{12}/Bi_2XO_6$ (X = Mo, W) hierarchical heterostructures exhibited a high visible light photocatalytic behavior for the decomposition of RB under visible light illumination, benefiting from the synergistic effects: (a) the large surface area and high efficiency of solar utilization resulting from the one-dimensional hierarchical heterostructures and (b) the heterojunction reducing the recombination of photogenerated electrons and holes by the photoinduced potential difference generated at the $Bi_4Ti_3O_{12}/Bi_2XO_6$ (X = Mo, W) heterojunction interface. These results indicated that the $Bi_4Ti_3O_{12}/Bi_2XO_6$ (X = Mo, W) hierarchical heterostructures are promising candidate materials for wastewater treatment. Also, we believe that this route would offer new insight into the design and fabrication of advanced materials with heterojunction structures for photocatalytic and optoelectronic applications.

References

[1] R. Asahi, T. Morikawa, T. Ohwaki, K. Aoki, Y. Taga, Science 293 (2001) 269–271.
[2] K. Maeda, K. Teramura, D. Lu, T. Takata, N. Saito, Y. Inoue, K. Domen, Nature 440 (2006) 295.
[3] X. Wang, J. Yu, Y. Chen, L. Wu, X. Fu, Environ. Sci. Technol. 40 (2006) 2369–2374.
[4] Z. Zou, J. Ye, K. Sayama, H. Arakawa, Nature 414 (2001) 625–627.
[5] M. Zhang, C. Shao, Z. Guo, Z. Zhang, J. Mu, P. Zhang, T. Cao, Y. Liu, ACS Appl. Mater. Interfaces 3 (2011) 2573–2578.
[6] M. Batzill, Energy Environ. Sci. 4 (2011) 3275–3286.
[7] D. Wang, G. Xue, Y. Zhen, F. Fu, D. Li, J. Mater. Chem. 22 (2012) 4751–4758.
[8] S. Sun, W. Wang, L. Zhang, E. Gao, D. Jiang, Y. Sun, Y. Xie, ChemSusChem 6 (2013) 1873–1877.
[9] K. Zhao, L. Zhang, J. Wang, Q. Li, W. He, J. Yin, J. Am. Chem. Soc. 135 (2013) 15750–15753.
[10] J. Jiang, K. Zhao, X. Xiao, L. Zhang, J. Am. Chem. Soc. 134 (2012) 4473–4476.
[11] J. Yu, A. Kudo, Adv. Funct. Mater. 16 (2006) 2163–2169.
[12] M. Shang, W. Wang, J. Ren, S. Sun, L. Zhang, Nanoscale 3 (2011) 1474–1476.
[13] G. Tian, Y. Chen, R. Zhai, J. Zhou, W. Zhou, R. Wang, K. Pan, C. Tian, H. Fu, J. Mater. Chem. A 1 (2013) 6961–6968.
[14] G. Tian, Y. Chen, W. Zhou, K. Pan, Y. Dong, C. Tian, H. Fu, J. Mater. Chem. 21 (2011) 887–892.
[15] C. Kongmark, R. Coulter, S. Cristol, A. Rubbens, C. Pirovano, A. Löfberg, G. Sankar, W. Beek, E. Bordes-Richard, R. Vannier, Crystal Growth Des 12 (2012) 5994–6003.
[16] G. Liu, L. Wang, H. Yang, H. Cheng, G. Lu, J. Mater. Chem. 20 (2010) 831–843.
[17] L. Zhang, H. Wang, Z. Chen, P. Wong, J. Liu, Appl. Catal. B Environ. 106 (2011) 1–13.
[18] W. Yao, X. Xu, H. Wang, J. Tao Zhou, X. Yang, Y. Zhang, S. Shang, B. Huang, Appl. Catal. B. Environ. 52 (2004) 109–116.

[19] H. Zhang, M. Lü, S. Liu, L. Wang, Z. Xiu, Y. Zhou, Z. Qiu, A. Zhang, Q. Ma, Mater. Chem. Phys. 114 (2009) 716–721.
[20] W. Zhao, Z. Jia, E. Lei, L. Wang, Z. Li, Y. Dai, J. Phys. Chem. Solids 74 (2013) 1604–1607.
[21] Y. Wang, Q. Wang, X. Zhan, F. Wang, M. Safdar, J. He, Nanoscale 5 (2013) 8326–8339.
[22] W. Zhao, Y. Jin, C. Gao, W. Gu, Z. Jin, Y. Lei, L. Liao, Mater. Chem. Phys. 143 (2014) 952–962.
[23] T. Cao, Y. Li, C. Wang, Z. Zhang, M. Zhang, C. Shao, Y. Liu, J. Mater. Chem. 21 (2011) 6922–6927.
[24] D. Hou, W. Luo, Y. Huang, J. Yu, X. Hu, Nanoscale 5 (2013) 2028–2035.
[25] Y. Xu, W. Zhang, Appl. Catal. B Environ. 140–141 (2013) 306–316.
[26] Y. Park, W. Kim, D. Monllor-Satoca, T. Tachikawa, T. Majima, W. Choi, J. Phys. Chem. Lett. 4 (2013) 189–194.
[27] S. Choi, S. Kim, S. Lim, H. Park, J. Phys. Chem. C 114 (2010) 16475–16480.
[28] J.F. Moulder, W.F. Stickle, P.E. Sobol, K.D. Bomben, in: J. Chastain (Ed.), Handbook of X-ray Photoelectron Spectroscopy, Perkin-Elmer Corporation, Eden Prairie, MN, 1992.
[29] C. Jovalekic, M. Pavlovic, P. Osmokrovic, L. Atanasoska, Appl. Phys. Lett. 72 (1998) 1051–1053.
[30] M. Chu, M. Ganne, M. Caldes, L. Brohan, J. Appl. Phys. 91 (2002) 3178–3187.
[31] V.S. Dharmadhikari, S.R. Sainkar, S. Badrinarayan, A. Goswami, J. Electron Spectrosc. Relat. Phenom. 25 (1982) 181–189.
[32] H. Deng, W. Hao, H. Xu, C. Wang, J. Phys. Chem. C 116 (2012) 1251–1255.
[33] A.B. Patil, K.R. Patil, S.K. Pardeshi, J. Solid State Chem. 184 (2011) 3273–3279.
[34] A. Brant, S. Yang, N. Giles, M. Zafar Iqbal, A. Manivannan, L. Halliburton, J. Appl. Phys. 109 (2011) 073711–073717.
[35] M. Zhang, C. Shao, J. Mu, Z. Zhang, Z. Guo, P. Zhang, Y. Liu, CrystEngComm 14 (2012) 605–612.
[36] S. Wang, Y. Song, L. Jiang, J. Photochem. Photobiol. C Photochem. Rev. 8 (2007) 18–29.
[37] R. Wang, K. Hashimoto, A. Fujishima, M. Chikuni, E. Kojima, A. Kitamura, M. Shimohigoshi, T. Watanabe, Nature 388 (1997) 431–432.